BULLETIN OF THE POLISH ACADEMY OF SCIENCES
TECHNICAL SCIENCES, Vol. 74(6), 2026, Article number: 5997
DOI: 10.24425/bpasts.2026.5997

Autonomous parafoil recovery path planning and deployment algorithm for fixed-wing UAVs

Nezar SAHBON*, Michał WELCER, Albert ZAJDEL, and Cezary SZCZEPAŃSKI

Łukasiewicz Research Network—Institute of Aviation, Al. Krakowska 110/114, 02-256 Warszawa, Poland

Abstract. Safe and accurate recovery of fixed-wing Unmanned Aerial Vehicles (UAVs) is a critical aspect of autonomous operations, especially for systems designed for hand or catapult launch, which may lack landing gear. Under these conditions, parachute systems are often used for a safe landing, although using these systems for precise recovery in populated areas, high terrain, and water presents significant challenges. In addition, weather conditions have a major impact on the descent path post-parachute deployment, further complicating landing within the designated safe zones. Improper location and timing of parachute deployment may risk large errors or unsafe touchdown, increasing the need for precise parachute deployment location and timing.

This study presents the development of an autonomous parafoil deployment and recovery path planning algorithm for fixed-wing UAVs. The proposed solution calculates the optimal parachute deployment point and generates a recovery trajectory that guides the UAV toward this point while ensuring appropriate deployment orientation with respect to the desired landing location. The algorithm integrates UAV flight states, the descent characteristics of the combined UAV-parachute system, and prevailing weather conditions to determine the deployment point and recovery trajectory. A simulation model of the algorithm, along with the UAV dynamic model, was developed in MATLAB/Simulink to investigate its performance. The results indicate that the proposed algorithm can improve UAV recovery strategies, minimising landing errors, and increasing operational safety within the considered simulation conditions. Future validation of the algorithm under real-world conditions may provide further insight into its reliability and lead to refinements in subsequent iterations.

Keywords: autonomous recovery; path planning; parachute deployment; fixed-wing UAV; guidance algorithm.

1. INTRODUCTION

Numerous domains have been revolutionised by the use of Unmanned Aerial Vehicles (UAVs), including surveillance, agriculture, logistics and military, by enabling real-time monitoring and efficient delivery [1–3]. However, the safe and efficient recovery of UAVs after a mission, particularly in emergency situations and when they lack conventional landing gear, remains a significant challenge. For fixed-wing UAVs, especially those designed for catapult or hand launch, landing on the runway may not be feasible. Thus, other recovery systems, such as parachute recovery systems or belly landings, have become increasingly significant for ensuring reliable recovery of UAV platforms. Parachute recovery systems, for instance, work well for emergency deployment and in regions with no designated runways. They offer the means for safe, reliable recovery in most environments. Parachute systems, nevertheless, introduce substantial challenges, especially where precise landings are required. Several missions necessitate precise landing in predefined safe zones, and such variables as wind conditions, aerodynamic design of the parachute-UAV system, parachute deployment time, and altitude must be taken into consideration in order to achieve such an objective. Wyllie [4] emphasises the importance of parachute recovery systems on unprepared terrain for tactical fixed-wing UAVs, with key considerations such as wind influence, descent environment, and accurate navigation systems. The study concludes that the integration of parachute systems with accurate wind models and deployment algorithms may enable safe, precise and automated recovery under various environmental conditions. Similarly, Fortier [5] focused on the improvement of airdrop systems for logistics purposes. The investigations were carried out on guided and unguided systems, which took into account the wind, parachute dynamics and release condition uncertainties. As a result, a tool was developed for the estimation of airdrop landing errors, leading to enhanced accuracy and predicted landing outcomes.

The number of parameters influencing the success rate of precise landing in a predefined location introduces a major challenge, which draws attention to the need for improved parachute deployment systems and algorithms capable of predicting the optimal deployment point and landing uncertainties. Recent advancements in software development and computational power enable modelling and simulation of aircraft motion alongside the parachute deployment and its physical effects on the flight [6]. This framework allows the analysis of various parachute models and deployment algorithms, thereby promoting advancements in automatic recovery systems. Modelling UAV dynamics with a recovery system such as a parachute is a complex task, taking into account various nonlinearities which can significantly impact the outcome. Several studies were conducted on the dynamic modelling of the combined parachute-vehicle system [7–10]. A study on autonomous landing employed a nu-

*e-mail: nezar.sahbon@ilot.lukasiewicz.gov.pl

Manuscript submitted 2026-03-16, revised 2026-08-14, initially accepted for publication 2026-09-07, published in November 2026.

© 2026 The Author(s). This is an open access article under the CC BY license (http://creativecommons.org/licenses/by/4.0/)

merical multi-body method for modelling the coupled vehicle-parachute system using a parafoil parachute [11]. This type of parachute offers several glide and manoeuvring capabilities compared to the classical circular parachute. Such abilities allow the steering of the coupled system, enabling higher landing accuracy. Furthermore, validation of the integrated system was demonstrated in the cited work by performing autonomous landing simulations under various conditions. In addition to autonomous landing systems, recent studies have investigated parafoil recovery and homing under wind disturbances [12–14]. For example, Tao *et al.* [15] proposed novel modelling methods to simulate parafoil flying under rain and wind conditions by establishing a dynamic model using revised aerodynamic equations based on Computational Fluid Dynamics (CFD). Zhao *et al.* [16] presented a nonlinear six-degree-of-freedom (6-DOF) model of the parafoil system based on aerodynamic parameter identification through airdrop tests, while further airdrop experiments verified the effectiveness of the dynamic model and the accuracy of the identification process. These studies, together with recent work on parafoil trajectory planning using a restricted 6-DOF model [17], form the foundation for further research that can enhance the accuracy of autonomous UAV recovery, which promotes the development of more integrated and predictive algorithms.

In addition, a study that focused on an affordable guided airdrop system (AGAS) presented a concept of a low-cost cargo air delivery system using a flat, solid, circular parachute and an actuator-induced canopy deformation to generate steering by shifting the centre of pressure. AGAS relied on wind estimations for computing the air release point, together with the control authority to overcome errors induced by the wind estimation and release-point calculations [18]. Wei *et al.* [19] proposed a closed-loop guidance and control framework for autonomous parafoil precision landing using a 6-DOF parafoil model, trajectory optimisation, and a Nonlinear Model Predictive Controller (NMPC)-based tracking. Their work demonstrated advanced trajectory generation and control post-parachute deployment, with flap deflections as main control inputs. However, the problem was formulated from the parafoil system itself and concentrated on terminal landing trajectory optimisation post-deployment. Moreover, recent studies have further investigated autonomous parafoil landing through model-predictive control, trajectory planning, and coordinated guidance and control methods [20, 21].

The previously cited research has addressed important aspects of parachute-based precision recovery such as parachute dynamic modelling, coupled parachute-vehicle system dynamics, autonomous parafoil landing, aerodynamic parameter identification, and environmental effects on precise recovery. Most studies related to parafoil modelling begin after the parafoil has already been deployed and mainly revolve around cargo delivery, payload release, and guided airdrops. However, the problem addressed in this manuscript differs from conventional parachute recovery studies, as the novelty of the presented work lies in the development of an integrated end-to-end framework for autonomous recovery of a fixed-wing UAV, including wind-aware parachute deployment point estimation, path planning toward the deployment point, automatic parachute deployment, transition from powered flight to parafoil descent, recovery at a predefined landing zone, and evaluation of controlled descent steering following parachute deployment. It is worth noting that the presented pre-deployment path-planning framework not only answers the question of where the parachute should be deployed, but also how a fixed-wing UAV should approach that deployment point so the system initiates the descent with a favourable orientation relative to the target landing point. This issue is particularly relevant for fixed-wing aircraft, unlike the airdrop systems presented in the literature.

Building upon the aforementioned research efforts and the challenges in precise UAV recovery, this study investigates the development of an autonomous parachute deployment algorithm designed for fixed-wing UAVs equipped with a parafoil parachute. The proposed framework aims to determine the optimal parachute deployment location by integrating the UAV flight dynamics, descent characteristics of the combined UAV-parachute system, and environmental conditions. In addition to computing the deployment point, the algorithm generates a recovery trajectory that guides the aircraft toward this point while ensuring a favourable deployment orientation with respect to the desired landing location. This trajectory planning step allows the UAV to approach the deployment point while aligning with the parafoil descent path, thereby improving landing accuracy. This research implements and evaluates the proposed solution within a simulation framework developed in the MATLAB/Simulink environment. This simulation-based development represents a foundational step toward assessing the potential performance of the proposed architecture. Moreover, performance was analysed under both controlled and uncontrolled descent scenarios. A set of Monte Carlo simulations was conducted with uncertainties introduced into the UAV and parachute aerodynamic coefficients, while the wind profile was included as a deterministic input to compare controlled and uncontrolled descent under fixed-wind conditions. This setup enables an assessment of deployment accuracy under aerodynamic-parameter uncertainty, offering crucial insights into the performance of the algorithm and its potential contribution to increased landing precision. In addition, the simulation provides a probabilistic view of possible outcomes, margins of error, and estimated confidence intervals.

The structure of the article is as follows: Section 2 introduces the vehicle model employed in the simulation. Section 3 presents the Model-In-the-Loop (MIL) simulation environment, including the dynamic model, the proposed parachute deployment algorithm, the recovery path planning algorithm, and the guidance logic. Afterwards, Section 4 presents the results of the study for Monte Carlo uncertainty analysis with the proposed algorithm and selected landing scenarios. Finally, the conclusions and future plans will be outlined in Section 5.

2. FOXTECH GREAT SHARK 330

The study utilises the FOXTECH Great Shark 330 UAV (See Fig. 1), a multi-purpose UAV primarily designed as a vertical take-off and landing (VTOL) system. However, due to the avail-



Fig. 1. FOXTECH Great Shark 330 UAV [22]

ability of aerodynamic properties of this vehicle, it was selected for the study under the assumption that only the fixed-wing configuration was used. This choice aligns with the study focus on fixed-wing UAVs and enables a straightforward analysis of the proposed parachute deployment and autonomous path planning algorithm and the landing accuracy as a result of its implementation.

The Great Shark 330 UAV selection was driven by its off-the-shelf availability, proven performance, and the availability of aerodynamic and geometric data, making it an appropriate representative platform for this study. Although the aircraft is capable of vertical take-off and landing, its VTOL capabilities were not utilised in the simulations. Instead, the vehicle was treated only in its fixed-wing configuration, consistent with the scope of the proposed recovery framework. Therefore, the use of the Great Shark 330 should be interpreted as a representative fixed-wing UAV case study, rather than as a platform-specific argument for adding parachute recovery to a VTOL aircraft. The proposed algorithm is intended as a generic recovery methodology for fixed-wing UAVs and is not limited to VTOL platforms. The main properties of this vehicle are outlined in Table 1.

Table 1
Great Shark 330 UAV properties [22, 23]

Parameter	Symbol	Value	Unit
Mass	m	20	kg
Mean aerodynamic chord	$\bar{c}$	0.286	m
Reference area	S_{ref}	0.7656	m^2
Wing span	b	3.3	m
Moment of inertia about the x-axis	I_{xx}	1.57	$\text{kg}\cdot\text{m}^2$
Moment of inertia about the y-axis	I_{yy}	2.43	$\text{kg}\cdot\text{m}^2$
Moment of inertia about the z-axis	I_{zz}	4.05	$\text{kg}\cdot\text{m}^2$

3. DYNAMIC MODEL

The simulation begins with the activation of the landing mode, where the proposed algorithm computes the desired parachute deployment position and the optimal path towards this point. The developed control algorithm keeps the UAV on the commanded path while maintaining the altitude; once it is within the specified threshold, the parachute is deployed and the engine is cut off. The parachute deployment introduces significant effects on the system dynamics, as the combined UAV-parachute system is treated as a single rigid dynamic object taking into account the added forces and moments from parachute deployment, in addition to the changes in mass and inertia due to the apparent effects of parachute deployment. The tension in the suspension cable and the pendulum motion between the UAV and the canopy were not modelled, but rather the most significant effects of the coupling were captured using the apparent mass/inertia and the aerodynamic forces due to the parachute. The framework developed in MATLAB/Simulink addresses this complex task by modelling the six degrees of freedom (6-DOF) nonlinear dynamics of the UAV using equations of motion including the parachute effects were outlined in equation (1) and equation (2).

$$m\left(\vec{V}_b + \vec{\omega}_b \times \vec{V}_b\right) = \vec{F}_A + \vec{F}_T + \vec{F}_G + \vec{F}_P\,, \tag{1}$$

$$I \cdot \vec{\dot{\omega}}_b + \vec{\omega}_b \times (I \cdot \vec{\omega}_b) = \vec{M}_A + \vec{M}_P\,, \tag{2}$$

where

- m – total mass of the UAV–parachute system, [kg];
- $\vec{V}_b$ – linear velocity vector expressed in the body-fixed frame, [m/s];
- $\vec{\dot{V}}_b$ – linear acceleration vector in the body-fixed frame, [m/s^2];
- $\vec{\omega}_b$ – angular velocity vector in the body-fixed frame, [rad/s];
- $\vec{\dot{\omega}}_b$ – angular acceleration vector in the body-fixed frame, [rad/s^2];
- I – inertia tensor of the UAV–parachute system expressed in the body-fixed frame, [kg m^2];
- $\vec{F}_A$ – aerodynamic force vector, [N];
- $\vec{F}_T$ – thrust force vector, [N];
- $\vec{F}_G$ – gravitational force vector, [N];
- $\vec{F}_P$ – parachute aerodynamic force vector, [N];
- $\vec{M}_A$ – aerodynamic moment vector, [Nm];
- $\vec{M}_P$ – parachute moment vector, [Nm].

The dynamic model was constructed in the flat-earth North-East-Down (NED) inertial coordinate system with respect to the centre of mass of the object. The point at which the landing mode was initiated was defined as the centre of the NED coordinate system in the X and Y directions $(0, 0)$. The attitude representation in space was based on quaternions to improve three-dimensional simulation accuracy, while the Euler angles were utilised for presenting the results and for computing the components of the gravitational force vector. The relationship between the inertial NED frame, the body-fixed frame $\text{O}_\text{b}\text{x}_\text{b}\text{y}_\text{b}\text{z}_\text{b}$, and the Euler angles ϕ, θ, ψ was presented in Fig. 2. Furthermore, the apparent mass and inertia effects resulting from parachute deployment must be taken into consideration when solving the equations of motion of the UAV-parachute system. These effects are caused by the interaction between the parachute and the fluid medium. Equation (3) defines the scalar total mass in

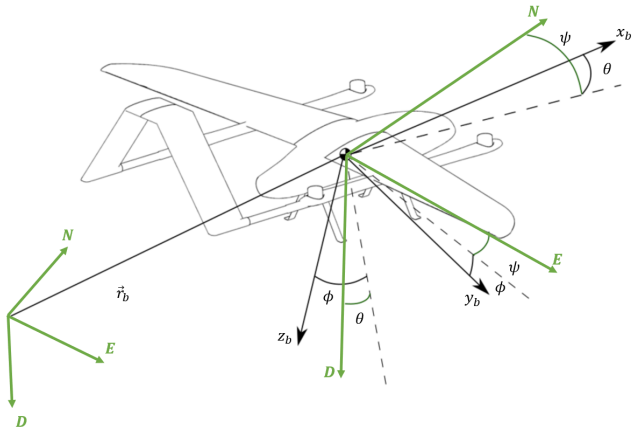

Fig. 2. Body-fixed frame $O_b x_b y_b z_b$, the flat-earth NED frame, and Euler angles

the implemented translational dynamics, comprising the mass of the UAV m_a, the deflated parachute mass m_p, and the effective scalar apparent-mass contribution obtained from the diagonal apparent-mass matrix. Similarly, equation (5) computes the total inertia of the system by combining the UAV inertia, the apparent inertia caused by the fluid-parachute interaction, and a simplified parallel-axis correction associated with the parachute attachment length. The parachute apparent mass and inertia contributions are given in equation (4) and equation (6), respectively. A rigid and fixed parafoil parachute was assumed for simplicity, with practical accuracy [24, 25].

$$m = m_a + m_p + \mathrm{tr}(M_{\mathrm{apparent}}), \tag{3}$$

where M_{apparent} is the diagonal apparent-mass matrix, and $\mathrm{tr}(M_{\mathrm{apparent}})$ represents the scalar apparent-mass contribution used in the implemented total-mass calculation. In the present implementation, the translational dynamics were formulated using a scalar total mass. Therefore, the directional apparent-mass terms were first calculated as the diagonal entries of the apparent-mass matrix and then combined into an effective scalar apparent-mass contribution. This approximation retains the additional inertial contribution associated with the parafoil-air interaction while keeping the translational mass formulation consistent with the implemented UAV-parachute dynamic model.

$$M_{\mathrm{apparent}} = \begin{bmatrix} 0.666\rho\left(1+\frac{8}{3}\bar{a}^2\right)t^2 b & 0 & 0 \\ 0 & 0.267\rho(t^2+2a^2(1-\bar{t}^2))c & 0 \\ 0 & 0 & 0.785\rho\,(1+2\bar{a}^2(1-\bar{t}^2))^{1/2}\left(\frac{\Lambda}{1+\Lambda}\right)bc^2 \end{bmatrix}, \tag{4}$$

where
ρ – air density, [kg/m^3];
$\bar{a}$ – parachute arc-to-span ratio, [–];
a – parachute arc height, [m];
t – parachute thickness, [m];
$\bar{t}$ – parachute thickness-to-chord ratio, [–];
b – parachute span, [m];
c – parachute chord, [m];
$\Lambda = b^2/S_{\mathrm{ref}}$ – parachute aspect ratio, [–];
S_{ref} – reference surface area of the parachute, [m^2];

$$I = I_{\mathrm{aircraft}} + I_{\mathrm{apparent}} + m_p\, l^2\, I_3\,, \tag{5}$$

where I_{aircraft} is the UAV inertia tensor, I_{apparent} is the apparent inertia tensor, l is the parachute attachment length, and I_3 is the 3×3 identity matrix. The term $m_p l^2 I_3$ represents a simplified diagonal parallel-axis correction accounting for the parachute mass being located at an effective offset from the UAV centre of mass. Since cable tension and pendulum dynamics were not explicitly modelled, the attachment length was used as the effective offset distance and the correction was applied equally to the principal inertia components.

$$I_{\mathrm{apparent}} = \begin{bmatrix} 0.055\rho c^2 b^3\left(\frac{\Lambda}{1+\Lambda}\right) & 0 & 0 \\ 0 & 0.0308\rho\left(\frac{\Lambda}{1+\Lambda}\right)c^4 b\left(1+\frac{\pi}{6}(1+\Lambda)\bar{a}^2\bar{t}^2\Lambda\right) & 0 \\ 0 & 0 & 0.0555\rho(1+8\bar{a}^2)b^3t^2 \end{bmatrix}. \tag{6}$$

The gravitational forces in the body-fixed reference frame were defined by equation (7), with an assumption of constant gravitational acceleration of $g = 9.81$ m/s^2 in the inertial reference frame.

$$\vec{F}_G = \begin{bmatrix} -m\,g\,\sin(\theta) \\ m\,g\,\cos(\theta)\,\sin(\phi) \\ m\,g\,\cos(\theta)\,\cos(\phi) \end{bmatrix}. \tag{7}$$

The aerodynamic forces and moments model was developed based on the stability and control derivatives of the Great Shark 330 UAV, obtained from the aerodynamic performance evaluation by Shah *et al.* [22]. The parachute model neglected attachment cable tension and pendulum effects to avoid overcomplicating the mathematical model. Therefore, assuming just the aerodynamic contribution greatly simplifies the problem, with balancing model fidelity and computational feasibility while still providing practically relevant results. The parachute aerodynamic model employed literature-based aerodynamic coefficients [26], omitting control derivatives. Although the aerodynamic coefficients from literature were derived for a parachute of different size, their use is justified since they are nondimensional flow behaviour and parafoil shape parameters rather than absolute dimensions. For calculation of resulting moments and forces, geometrical characteristics of the parafoil parachute employed in this study (listed in Table 2) were used. This approach acts in accordance with standard aerodynamic practices, commonly employed in early-stage performance evaluation when wind tunnel, Computational Fluid Dynamics (CFD), empirical or flight test results are unavailable.

Finally, the International Standard Atmosphere (ISA) Simulink model calculated the air density and speed of sound with respect to flight altitude. The wind environment was modelled using a horizontal wind profile, interpolating both speed and heading as a function of altitude.

Table 2
Primary characteristic properties of the parafoil parachute used in this study

Parameter	Symbol	Value	Unit
Mass	m_p	1.9	kg
Chord	c	1.92	m
Span	b	3.31	m
Parafoil panel thickness	t	0.25	m
Arc height	a	0.3	m
Attachment length	l	3	m
Surface area	S_{ref}	6.32	m^2

3.1. Model limitations and practical considerations

Several modelling assumptions were introduced in the study for balancing the model fidelity, computational efficiency and the primary objective of the proposed framework, which is necessary for a preliminary evaluation of a parafoil deployment and recovery path planning algorithm within a simulation environment. As previously mentioned, the suspension line tension dynamics and pendulum motion between the parafoil canopy and the UAV were neglected. Similar modelling assumptions have been adopted in previous parafoil modelling studies where the connection between canopy and payload was often treated as rigid and the system was described using a 6-DOF formulation [16,27]. In reality, these effects may introduce higher-order transient attitude variations, oscillatory behaviour, vortex-induced vibrations, and changes in the effective aerodynamic forces acting on the combined system. Although neglecting these effects simplifies the mathematical formulation and facilitates efficient simulations, it may also lead to optimistic estimations of landing accuracy, especially in the presence of turbulent atmospheric conditions. Nevertheless, the guidance and control framework presented takes into account the most significant coupling effects through the inclusion of parafoil aerodynamic forces, moments, apparent mass, and apparent inertia terms. The presented framework is intended to provide a first-order assessment of deployment-point computation and recovery-path planning, which justifies the adopted modelling simplifications.

Secondly, the transient parachute inflation process post-deployment was not explicitly modelled. Instead, a first-order transfer function was used to delay the onset of parachute aerodynamic effects. This simplification does not fully capture the highly nonlinear inflation process and the associated deployment loads that may occur during parachute opening.

Another significant assumption involves wind data availability and modelling. The computations of the deployment point in this study are based on a predefined horizontal wind profile as a function of altitude. Wind profiles are usually subject to uncertainties in their measurements and variability with respect to time. In practice, wind profile estimations may be obtained from onboard wind-estimation algorithms, meteorological forecasts, atmospheric databases, or ground-based measurements. Previous studies have demonstrated real-time wind estimation for fixed-wing UAVs using standard onboard sensors [28]. Thus, any error in measuring wind profiles will have a direct impact on the predicted drift and the accuracy of the computed deployment point. Therefore, the reported landing performance can be treated as an upper-bound estimation of operational performance under the assumption of wind knowledge. Finally, the proposed approach has been evaluated through numerical simulations, incorporating six-degree-of-freedom vehicle dynamics, parafoil aerodynamic effects, apparent inertial effects, atmospheric modelling, and uncertainty analysis; experimental validation was beyond the scope of the presented study. Future work will focus on incorporating higher-fidelity coupled UAV-parafoil dynamics, improved wind estimation techniques, and experimental validation to further assess the practical applicability of the proposed recovery strategy.

3.2. Parachute deployment algorithm

The parachute deployment algorithm was designed to compute the deployment location necessary for a safe landing of the system at a predefined point. The algorithm computes the parachute deployment point (see equation (8)) by applying a drift of ΔX and ΔY to the target landing location denoted by $\vec{P}_T = [X_T, Y_T]^T$. The total drift was decomposed into two primary drift components: the parachute glide drift and wind drift, as denoted by equation (9).

$$\begin{bmatrix} X_{\text{deploy}} \\ Y_{\text{deploy}} \end{bmatrix} = \begin{bmatrix} X_T - \Delta X \\ Y_T - \Delta Y \end{bmatrix}, \tag{8}$$

$$\begin{bmatrix} \Delta X \\ \Delta Y \end{bmatrix} = \begin{bmatrix} \Delta X_{\text{PGD}} + \Delta X_{\text{wind}} \\ \Delta Y_{\text{PGD}} + \Delta Y_{\text{wind}} \end{bmatrix}. \tag{9}$$

Firstly, the parachute glide drift (PGD) in the X and Y directions was calculated by equation (10). This drift is largely determined by the dimensionless glide ratio of the combined parachute UAV system G_D, the vertical descent interval between the deployment and ground altitudes, and the heading towards the desired landing location, computed by equation (11). In general, the heading angle ψ_T would usually be computed using the relative position between the desired landing point and the UAV's position at landing mode initiation. However, since the landing sequence in this study starts at the origin $(0,0)$, this simplification removes the need for offset terms in equation (11).

$$\begin{bmatrix} \Delta X_{\text{PGD}} \\ \Delta Y_{\text{PGD}} \end{bmatrix} = \int_0^{z_{\text{deploy}}} G_D \begin{bmatrix} \cos(\psi_T) \\ \sin(\psi_T) \end{bmatrix} \mathrm{d}z, \tag{10}$$

where z_{deploy} denotes the parachute deployment altitude. Since G_D is dimensionless, the integration from the terrain level to the parachute deployment altitude gives the horizontal glide distance in metres.

$$\psi_T = \text{atan2}(Y_T, X_T). \tag{11}$$

A crucial component of the parachute deployment algorithm is the approximation of the descent drift caused by wind condi-

tions. This was done by integrating the wind profile ($V_{\text{wind}_{x,y}}$), computed using equation (12), with the descent rate of the UAV-parachute system $\bar{W}$ from the terrain level to the parachute deployment altitude z, defined by equation (13). The equations used here for computing the wind drift follow the version presented by Cacan *et al.* [29] in a form suitable for parafoil modelling. It is worth noting that in equation (12), ψ_{wind} is expressed in the horizontal NED frame and denotes the direction of the horizontal wind-velocity vector, measured from the positive north axis toward the positive east axis. Therefore, V_{wind_x} and V_{wind_y} correspond to the north and east wind-velocity components, respectively.

$$\begin{bmatrix} V_{\text{wind}_x}(z) \\ V_{\text{wind}_y}(z) \end{bmatrix} = \begin{bmatrix} V_{\text{wind}}(z)\cos(\psi_{\text{wind}}(z)) \\ V_{\text{wind}}(z)\sin(\psi_{\text{wind}}(z)) \end{bmatrix}, \tag{12}$$

where
$V_{\text{wind}}(z)$ – wind speed as function of altitude, [m/s];
$\psi_{\text{wind}}(z)$ – wind direction as function of altitude, [°];

$$\begin{bmatrix} \Delta X_{\text{wind}} \\ \Delta Y_{\text{wind}} \end{bmatrix} = \begin{bmatrix} \int_0^z \frac{V_{\text{wind}_x}}{\bar{W}}\,\mathrm{d}z \\ \int_0^z \frac{V_{\text{wind}_y}}{\bar{W}}\,\mathrm{d}z \end{bmatrix}. \tag{13}$$

Finally, both the glide performance coefficient G_D and the mean descent rate $\bar{W}$ of the combined UAV-parachute system were initially obtained through simulation by disabling the wind model and analysing the steady-state descent behaviour after the transient parachute deployment phase. However, additional simulations revealed that the vertical descent rate varies slightly with wind speed due to changes in the aerodynamic equilibrium of the integrated system. Consequently, the descent rate was modelled as a function of wind speed using linear interpolation between the simulated operating points. The descent rate values were set between 3 m/s at zero wind speed and approximately 3.75 m/s at 15 m/s wind speed. The glide ratio was estimated from the lift-to-drag ratio of the coupled UAV–parachute system, which yielded a glide ratio of $G_D = 3.31$ by averaging the lift-to-drag ratio over the quasi-steady descent phase following the transient parachute deployment response.

3.2.1. Recovery path planning to the deployment point

Upon computing the desired parachute deployment point $\vec{P}_{\text{deploy}}$, a recovery trajectory was created to guide the aircraft towards the deployment point while ensuring a favourable parachute deployment direction to the desired landing location $\vec{P}_{\text{target}}$. The trajectory path consists of a straight segment from the UAV position $\vec{P}_0$ at the recovery initiation trigger to a tangential entry point on a circular arc of radius R_{turn}, followed by a circular arc ending at $\vec{P}_{\text{deploy}}$. Several parameters must be defined for the path planning procedure, including the forward-cone threshold θ_{cone}, the number of candidate circles N_{circles}, and the weighting coefficients W_{dist} and W_{heading} used in the trajectory selection cost function. The complete recovery trajectory generation method is presented in Algorithm 1.

Algorithm 1: Optimal recovery trajectory generation toward the deployment point

Require: UAV position $\vec{P}_0$, heading ψ_0, deployment point $\vec{P}_{\text{deploy}}$, target point $\vec{P}_T$, turning radius R_{turn}, cone angle θ_{cone}, wind magnitude $|V_{\text{wind}}|$, weights W_{dist} and W_{heading}
Ensure: Optimal recovery trajectory $\vec{P}^*$

Compute direction to deployment point $\hat{\mathbf{d}}_{\text{deploy}}$ and UAV heading vector $\hat{\mathbf{h}}_0$
Compute heading deviation α_{deploy}
if $|\alpha_{\text{deploy}}| \le \theta_{\text{cone}}$ and $|V_{\text{wind}}|$ is negligible **then**
    Set $\vec{P}^*$ as the straight-line trajectory from $\vec{P}_0$ to $\vec{P}_{\text{deploy}}$
    return $\vec{P}^*$
end if
Compute desired deployment-to-target direction $\hat{\mathbf{d}}_{DT}$
Generate N_{circles} candidate circle centres $\vec{C}_i$ around $\vec{P}_{\text{deploy}}$
Compute target heading ψ_T from $\vec{P}_{\text{deploy}}$ to $\vec{P}_T$
for each candidate circle centre $\vec{C}_i$ **do**
    Compute distance $d_i = \|\vec{C}_i - \vec{P}_0\|$
    if $d_i < R_{\text{turn}}$ **then**
        Discard candidate
        continue
    end if
    Compute left and right tangent solutions from $\vec{P}_0$ to the circle
    for each turn direction $k \in \{L, R\}$ **do**
        Compute entry point $\vec{P}^k_{\text{entry}}$
        Construct candidate trajectory $\vec{P}^k_i$ from a straight segment and a circular arc
        Compute exit heading ψ^k_{exit} at $\vec{P}_{\text{deploy}}$
        Evaluate trajectory cost

$$J_i^k = W_{\text{dist}}(d_i + R_{\text{turn}}) + W_{\text{heading}} R_{\text{turn}} \left|\psi^k_{\text{exit}} - \psi_T\right|$$

    end for
end for
Select the candidate trajectory with minimum cost:

$$\vec{P}^* = \arg\min_{i,k} J_i^k$$

return $\vec{P}^*$

3.2.2. Guidance and control

The guidance module then generated the desired roll angle continuously to track the planned recovery trajectory towards the deployment point and then to the desired landing point post-parachute deployment. The lateral motion of the fixed-wing UAV was primarily fulfilled through bank-induced turning; the roll command formed the principal control signal for path following during the pre-deployment phase with minor corrections post-deployment. Regarding the pitch command, the guidance algorithm maintains the altitude of the aircraft upon triggering the recovery phase. However, post-parachute deployment, the pitch and yaw controls are disabled. The guidance through the generated desired path followed the L_1 guidance logic [30]. The guidance starts by computing the line segment of the current

path between the previous waypoint and the next waypoint vectors denoted by $\vec{W}_{PA}$ and $\vec{W}_{PB}$ respectively (see equation (14)).

$$\vec{n} = \frac{\vec{W}_{PB} - \vec{W}_{PA}}{\|\vec{W}_{PB} - \vec{W}_{PA}\|}. \tag{14}$$

To compute the L_1 guidance distance, one must specify a damping ratio ζ and turn period T_L. These parameters greatly influence the track guidance performance and are aircraft-dependent. Moreover, the ground speed magnitude was needed in addition to compute the L_1 distance using the following equation:

$$L_1 = \frac{\zeta T_L V_g}{\pi}. \tag{15}$$

To ensure a real forward lookahead distance of the guidance point, the lookahead distance L_1 must be constrained using the cross-track error magnitude $\|\vec{e}_{\text{crosstrack}}\|$ and the minimum forward distance as:

$$L_1 = \max\left(L_1, \sqrt{\|\vec{e}_{\text{crosstrack}}\|^2 + l_{\text{fwd,min}}^2}\right). \tag{16}$$

Computing the cross-track error magnitude first required defining the vector from the start point of the current segment to the aircraft position $\vec{P}$, denoted by $\vec{w}$ and computed via equation (17). This was then used to find the perpendicular cross-track error vector by projecting $\vec{w}$ on to $\vec{n}$ using equation (18).

$$\vec{w} = \vec{P} - \vec{W}_{PA}, \tag{17}$$

$$\vec{e}_{\text{crosstrack}} = \vec{w} - (\vec{w} \cdot \vec{n})\vec{n}. \tag{18}$$

Next, it was necessary to compute the angle η between the ground track and target waypoint bearing. This can be done by calculating the angular deviation between the normalised ground speed vector $\hat{v}_g$ and the normalised error vector $\hat{l}$ between the current position and the lookahead reference point $\vec{P}_{L1}$ (see equation (19) through equation (21)).

$$\vec{P}_{L1} = \left(\vec{W}_{PA} + (\vec{w} \cdot \vec{n})\vec{n}\right) + \left(\sqrt{L_1^2 - \|\vec{e}_{\text{crosstrack}}\|^2}\right)\vec{n}, \tag{19}$$

$$\hat{v}_g = \frac{\vec{v}_g}{\|\vec{v}_g\|}, \tag{20}$$

$$\hat{l} = \frac{\vec{P}_{L1} - \vec{P}}{\|\vec{P}_{L1} - \vec{P}\|}. \tag{21}$$

By taking the four-quadrant inverse tangent function, the signed angular deviation can be found using the atan2 formulation, which ensures robust numerical computation, correctly distinguishing clockwise and counter-clockwise deviations (see equation (22)).

$$\eta = \text{atan2}(\sin(\eta), \cos(\eta)) \qquad \eta \in [-\pi, \pi], \tag{22}$$

where $\cos(\eta) = \hat{v}_x\hat{l}_x + \hat{v}_y\hat{l}_y$, $\sin(\eta) = \hat{v}_x\hat{l}_y - \hat{v}_y\hat{l}_x$.

Finally, the commanded lateral acceleration was determined with equation (23), plugging the commanded acceleration along with the gravitational acceleration magnitude g into equation (24) yields the commanded roll angle.

$$a_{cmd} = \frac{2v_g^2 \sin(\eta)}{L_1}, \tag{23}$$

$$\phi_{cmd} = \text{atan2}(a_{cmd}, g), \qquad \phi_{cmd} \in [\phi_{\min}, \phi_{\max}]. \tag{24}$$

An autopilot control loop was developed for the study, with proportional-integral-derivative (PID) controllers used for the roll, pitch and yaw channels. While the UAV stayed on the desired path, its speed was maintained at a cruise condition of 22 m/s. This was done via a dedicated PID controller that adjusted the thrust output along the x-axis to maintain the desired airspeed.

As previously mentioned, the parafoil-UAV was regarded as a single coupled rigid body with modified aerodynamic, apparent mass, and apparent inertia properties post-parachute deployment. Hence, the post-parachute dynamics were not treated as a conventional fixed-wing flight, as the engine was turned off and the forward speed was reduced. Rather, the resultant aerodynamic forces and moments were governed by the parachute-UAV system configuration. The available control authority was therefore inherently reduced compared to the pre-deployment phase as a result of the lower forward speed of the combined system following engine shutdown and parachute deployment. This modelling framework assumed that the aircraft ailerons maintained limited residual control authority over the roll channel of the combined system. The roll motion of the aircraft changes the orientation of the resultant aerodynamic force vector, producing a lateral component that enables minimal course adjustment during the controlled descent phase [27,31]. To avoid the assumption of excessive post-deployment manoeuvrability, the commanded roll angle was constrained to 10°. Therefore, the controlled descent case should be interpreted as an assessment of the potential benefit of limited post-deployment roll authority within the adopted model, rather than as experimental validation of a specific actuator layout. This model-in-the-loop structure enabled simulation of the parafoil-UAV system, including the parachute deployment algorithm, path planning and subsequent landing, while accounting for nonlinear dynamics, atmospheric effects, and control logic transitions.

4. NUMERICAL RESULTS

Performance analysis of the parachute deployment algorithm was carried out through numerical simulations in the MATLAB/Simulink environment, using a Runge-Kutta 4th-order (RK4) solver at a 200 Hz integration frequency. In this study, a Monte Carlo analysis was conducted to evaluate the landing dispersion, introducing uncertainties in the parachute and UAV aerodynamic parameters. Particularly, the analysis considered an uncertainty of 5% for the UAV aerodynamic derivatives and 10% for the parachute aerodynamic derivatives, with 1 000 simulations performed for each descent scenario. The selected aerodynamic parameters were independently perturbed

as $p = p_0(1+\delta)$, where p is the perturbed parameter value, p_0 is its nominal value, and $\delta \sim \mathcal{U}(-0.05, 0.05)$ for the UAV derivatives and $\delta \sim \mathcal{U}(-0.10, 0.10)$ for the parachute derivatives. The randomized UAV parameters included C_{D0}, $C_{D\alpha}$, $C_{D\alpha^2}$, $C_{Y\beta}$, C_{L0}, $C_{L\alpha}$, $C_{l\beta}$, C_{m0}, $C_{m\alpha}$, and $C_{n\beta}$, while the randomized parachute parameters included C_{D0}, $C_{D\alpha}$, $C_{Y\beta}$, C_{L0}, $C_{L\alpha}$, $C_{l\beta}$, C_{lp}, C_{m0}, $C_{m\alpha}$, C_{mq}, and $C_{n\beta}$. Moreover, control-surface derivative uncertainty was set to zero and was therefore not included in the Monte Carlo randomization. The wind profile was included as a deterministic input and was kept identical for the controlled and uncontrolled Monte Carlo cases. The wind profile was defined at altitude levels $h_{\text{wind}} = [0, 100, 600]$ m, with wind speeds $V_{\text{wind}} = [5, 3, 3]$ m/s and wind-direction angles $\psi_{\text{wind}} = [-60, -30, -150]^\circ$ in the NED frame. Wind-speed and wind-direction uncertainty were not randomized, since the objective of this analysis was to isolate the influence of aerodynamic-parameter uncertainty and active roll steering. Two primary descent scenarios were assessed: uncontrolled and controlled. The uncontrolled scenario disabled all control surfaces upon parachute deployment, allowing the system to descend under the influence of the deterministic wind profile and passive glide behaviour. On the other hand, the controlled case maintained aileron control actuation to influence the roll channel, allowing the system to steer toward the desired landing point during descent. These cases were designed to isolate the impact of active control on parachute descent accuracy, highlighting its contribution to autonomous precision landing under the assumed aerodynamic-uncertainty and fixed-wind conditions.

All desired landing points were defined in the flat-earth NED coordinate system, with the landing mode initiation location set as the origin $(0,0)$. The dispersion analysis reference desired landing point was placed at 2 000 metres north and 2 000 metres due east relative to the UAV. Moreover, the reference point fell within an ideal square-shaped 100 by 100 metres safe zone. This safe zone was nested within a larger acceptable zone measuring 300×300 metres, which in turn was enclosed by a 700×700 metres zone deemed unacceptable for safe landing due to the possible presence of objects which may damage the UAV. Landings outside this outer zone were considered damaging to the UAV. The initial altitude for all simulations was set to 250 metres.

The wind profiles were inspired by publicly available meteorological data obtained from Windy.com [32], where wind information is available at discrete altitude levels, including 0 m, 100 m, and 600 m. The selected altitude levels were kept in the model, despite the fact that the simulations presented in this study were initiated at 250 metres altitude and therefore primarily utilised the lower portion of the wind profile, with in-between wind values obtained through linear interpolation between the discrete altitude levels. Moreover, for the path planning and guidance, Table 3 outlined the values of the user-defined constants.

The dispersion results for the uncontrolled scenario were shown in Fig. 3, with its corresponding histogram in Fig. 4. The controlled scenario outcomes were presented in Fig. 5 and Fig. 6. A statistical summary of the landing performance, including the mean error $\bar{e}$, standard deviation σ, margin of error

Table 3
User-defined parameters for path planning and guidance

Parameter	Symbol	Value	Unit
Weighted distance coeff.	W_{dist}	1	–
Weighted heading coeff.	W_{heading}	3	–
Guidance response period	T_L	30	s
Guidance damping ratio	ζ	0.7	–
Number of circle candidates	N_{circles}	12	–
Maximum angle for the straight path	θ_{cone}	20	°
Path planning turn radius	R_{turn}	500	m
Maximum roll angle (pre-deployment)	$\phi_{\max}$	20	°
Maximum roll angle (post-deployment)	$\phi_{\max}$	10	°

E from the mean, and the 95% confidence interval, was provided in Table 4 for both scenarios. In addition, the percentage of Monte Carlo runs falling within each landing zone was reported in Table 5 to provide a safety-oriented interpretation of the dispersion results.

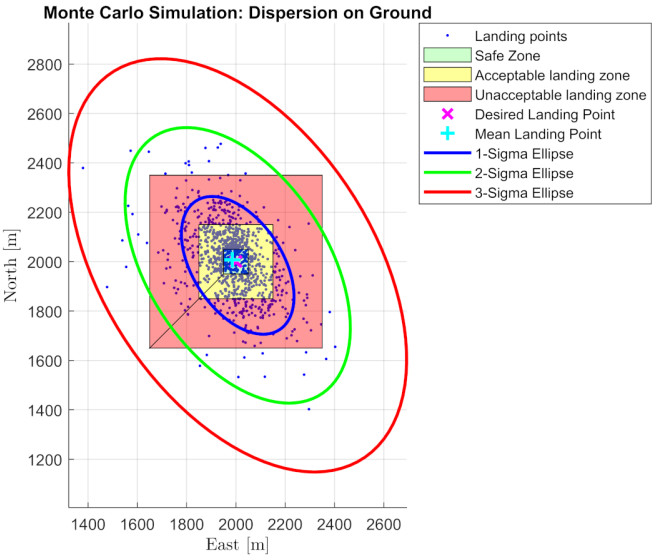

Fig. 3. Uncontrolled descent Monte Carlo dispersion results under uncertainty

Table 4
Monte Carlo dispersion statistical summary

	$\bar{e}$ [m]	σ [m]	E [m]	95% Confidence interval [m]
Uncontrolled descent	148.87	102.89	6.37	[142.49, 155.24]
Controlled descent	68.99	61.69	3.82	[65.16, 72.81]

The zone percentages in Table 5 were calculated using mutually exclusive square-zone boundaries, where the acceptable zone excludes the safe zone, and the unacceptable zone excludes both the safe and acceptable zones.

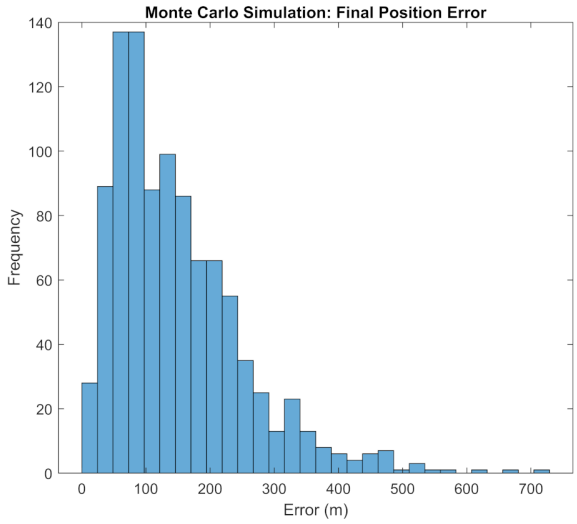

Fig. 4. Uncontrolled descent Monte Carlo dispersion histogram

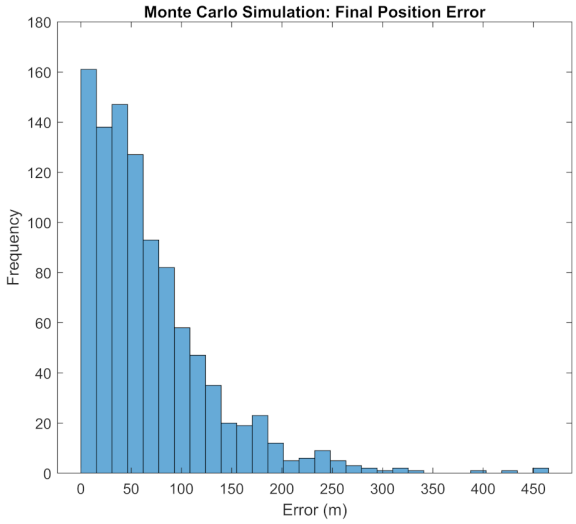

Fig. 6. Controlled descent Monte Carlo dispersion histogram

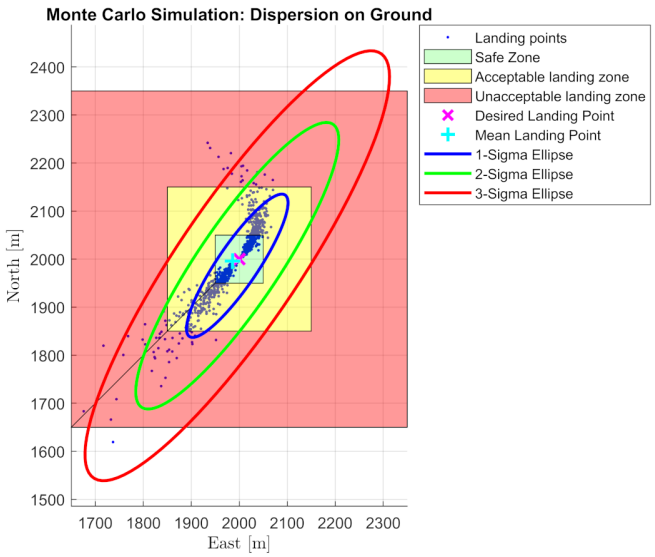

Fig. 5. Controlled descent Monte Carlo dispersion results under uncertainty

Table 5
Monte Carlo landing-zone classification

Zone	Uncontrolled [%]	Controlled [%]
Safe zone	15.10	56.90
Acceptable zone	50.20	37.00
Unacceptable zone	31.40	6.00
Outside outer zone	3.30	0.10

The dispersion plots show the desired landing point marked in magenta (×) and the mean landing point in cyan (+). The desired safe (green), acceptable (yellow), and unacceptable (red) landing zones were illustrated with increasing tolerance levels. Ellipses representing the 1-sigma (blue), 2-sigma (green), and 3-sigma (red) confidence intervals of the landing point distribution were also illustrated in the figures. The results clearly highlight the advantages of autonomous controlled descent, with a reduction of the mean landing error by approximately 53.65% compared to the uncontrolled descent. Notably, the average landing location falls within the designated safe zone, exhibiting high landing accuracy. The landing-zone classification further confirms the benefit of active steering. In the uncontrolled case, 15.10% of the Monte Carlo runs landed within the safe zone, while 3.30% landed outside the outer zone. In contrast, the controlled case increased the safe-zone percentage to 56.90% and reduced the percentage of landings outside the outer zone to 0.10%. This underscores the potential benefit of incorporating active steering within the proposed framework under the assumed simulation conditions.

It should be noted that the comparison between the uncontrolled and controlled descent Monte Carlo analyses was meant to isolate the contribution of active steering within the proposed framework. The Monte Carlo analysis demonstrated that the controlled descent reduced the mean landing error and the landing point dispersion relative to the uncontrolled descent. A similar trend was observed in guided airdrop studies, where active control resulted in lower landing errors relative to unguided descent [5]. Therefore, the presented comparison underlines the benefit of active steering within the proposed framework. However, this does not establish explicit superiority over alternative parafoil guidance and control strategies available in the literature.

Following the Monte Carlo analysis, controlled descent performance was further assessed for three distinct desired landing locations positioned at different bearings relative to the UAV's position upon initiating the landing mode. These scenarios were denoted as Cases A, B, and C, located at the coordinates (X_T, Y_T) provided in Table 6, along with the associated wind profiles (altitude h_{wind}, wind speed V_{wind}, and wind direction ψ_{wind}) and the resulting landing error for each case. Each point was enclosed by a 100 by 100 metre box designated as the safe zone. The

landing performance trajectory results for cases A to C were shown in Fig. 7 through Fig. 12.

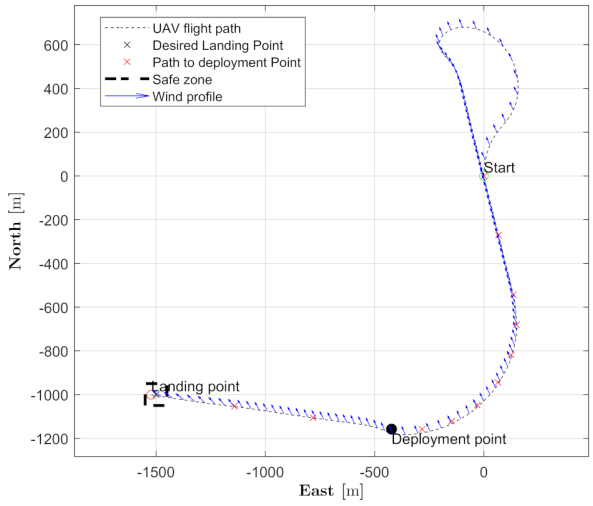

Fig. 7. Case A: Two-dimensional trajectory

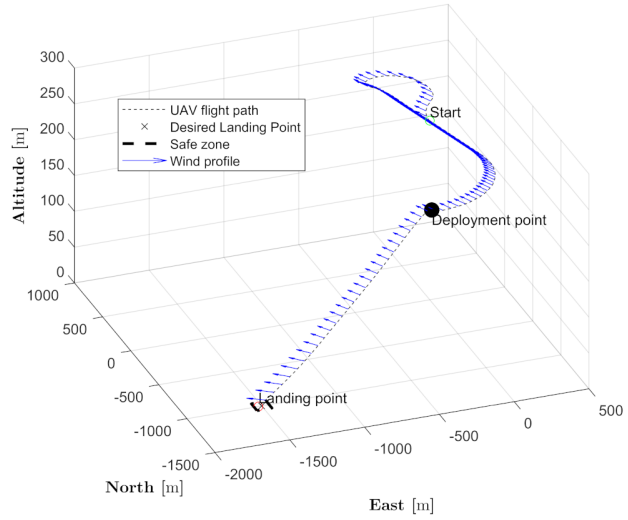

Fig. 8. Case A: Three-dimensional trajectory

The controlled landing results demonstrated the capability of the parachute deployment algorithm with controlled descent across various preferred points and wind conditions. In all three cases, the UAV successfully landed within the designated safe zone around each target coordinate. Case B achieved the highest

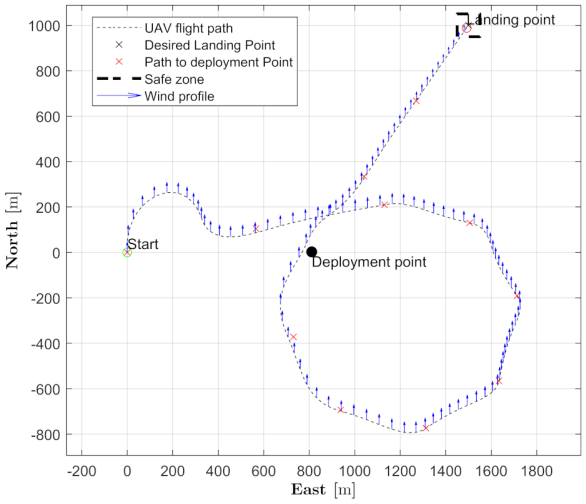

Fig. 9. Case B: Two-dimensional trajectory

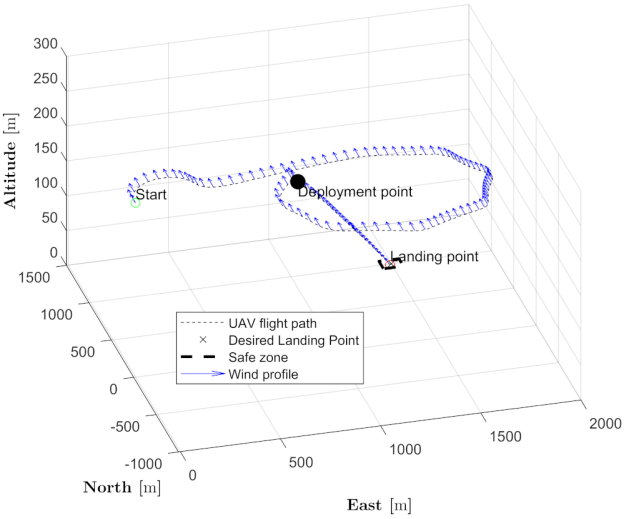

Fig. 10. Case B: Three-dimensional trajectory

accuracy with a final error of 13.94 metres, with the lowest wind speed scenario across the operational altitude levels during the descent and a target landing point in the north-east quadrant. Case C exhibited the highest deviation with a final error of 30.51 m, likely due to the additional turning manoeuvres required to reach the deployment point, though it still remained well within the defined safe zone. Case A featured the maximum wind speed at the ground layer and 10 m/s at the remaining layers, resulting in 22.53 metres of error, indicating a safe landing.

Table 6
Controlled landing test cases setup and final position error

	$[X_T, Y_T]$ [m]	h_{wind} [m]	V_{wind} [m/s]	ψ_{wind} [°]	Error [m]
Case A	$[-1000, -1500]$	$[0, 100, 600]$	$[12, 10, 10]$	$[-60, -30, -10]$	22.53
Case B	$[1000, 1500]$	$[0, 100, 600]$	$[5, 7, 12]$	$[0, 0, 0]$	13.94
Case C	$[2000, 0]$	$[0, 100, 600]$	$[10, 10, 10]$	$[90, 60, 45]$	30.51

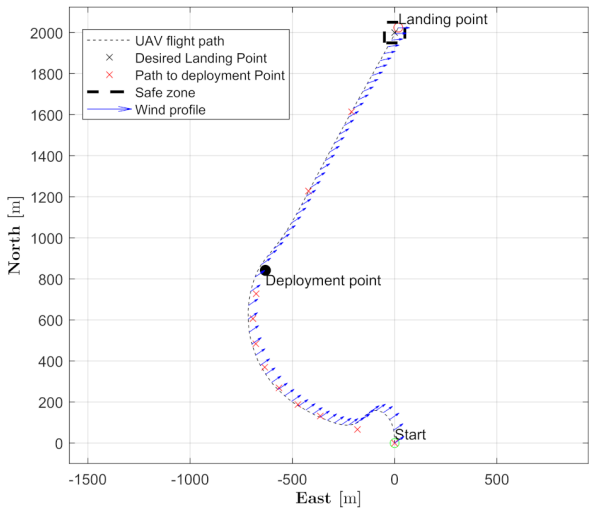

Fig. 11. Case C: Two-dimensional trajectory

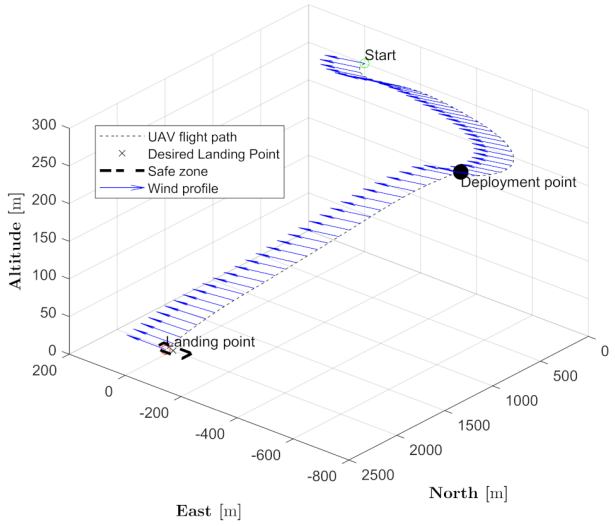

Fig. 12. Case C: Three-dimensional trajectory

These results suggest that the parafoil parachute deployment algorithm and path planning with active steering are capable of achieving precision landings within the considered simulation scenarios, parameter uncertainties, wind-profile assumptions, and modelling simplifications. Furthermore, the final position errors remain consistently within the safe zone threshold, underscoring the algorithm's resilience and adaptability to variable desired landing locations.

5. SUMMARY AND CONCLUSIONS

In this research, the numerical model of the Foxtech Great Shark 330 UAV descent using a parafoil parachute was developed, including aerodynamic and inertial effects resulting from parachute deployment and interaction with the air. A parachute deployment algorithm was successfully developed and implemented within the simulation model.

The results of the Monte Carlo dispersion analysis indicated the effectiveness of the proposed algorithm under the considered uncertainty assumptions. The controlled descent scenario with active roll steering improved the mean landing error by 53.65% in comparison with the uncontrolled descent case. The landing-zone classification further showed that active steering increased the percentage of Monte Carlo runs within the safe zone from 15.10% to 56.90%, while reducing landings outside the outer zone from 3.30% to 0.10%. The statistical analysis demonstrated a narrower dispersion for the controlled system with higher accuracy and tighter confidence intervals, indicating improved robustness of the controlled descent strategy within the considered simulation scenarios and uncertainty assumptions.

Further evaluations were carried out with active descent steering for various desired landing points at distinct headings and wind profiles, demonstrating the system's adaptability across the considered operating conditions. In all the simulation cases, the algorithm successfully computed the parachute deployment point with path planning in order for the UAV to land within the specified safe zone, with the final error ranging from 13.94 to 30.51 metres, under the considered wind-profile cases. These results showcase that the proposed parachute deployment algorithm and active descent steering may provide a feasible approach for improving recovery accuracy of UAV systems. The objective of this study was not to demonstrate superiority over existing guidance or control approaches that may be feasible for this type of problem, but rather to present a unified framework adapted to fixed-wing UAV operations. Moreover, the proposed framework was formulated using relatively computationally efficient guidance, path-planning, and deployment point estimation algorithms, facilitating implementation, reproduction, future improvements, and adaptation to onboard fixed-wing UAV recovery applications. To conclude, the presented approach demonstrates the potential of autonomous parachute deployment and path planning for improving fixed-wing UAV recovery performance within a simulation environment.

Further expansion upon this research will include integration with onboard sensors and experimental validation of the proposed solution. Future research will focus on increasing model fidelity, taking into consideration cable tension, pendulum motion dynamics, canopy inflation transients, wind estimation uncertainty, and turbulent wind profiles. In addition, hardware-in-the-loop evaluation and flight testing remain important directions for future work.

ACKNOWLEDGEMENTS

This research received no external funding.

REFERENCES

[1] P. Radoglou-Grammatikis, P. Sarigiannidis, T. Lagkas, and I. Moscholios, "A compilation of UAV applications for precision agriculture," *Comput. Netw.*, vol. 172, p. 107148, 2020, doi: 10.1016/j.comnet.2020.107148.

[2] B. Fan, Y. Li, R. Zhang, and Q. Fu, "Review on the technological development and application of UAV systems," *Chin. J. Electron.*, vol. 29, no. 2, pp. 199–207, 2020, doi: 10.1049/cje.2019.12.006.

[3] G.E. Jeler, "Military and civilian applications of UAV systems," in *International Scientific Conference Strategies XXI: The Complex and Dynamic Nature of the Security Environment*. Carol I National Defence University Publishing House, 2019, pp. 379–386.

[4] T. Wyllie, "Parachute recovery for UAV systems," *Aircr. Eng. Aerosp. Technol.*, vol. 73, no. 6, pp. 542–551, 2001, doi: 10.1108/00022660110696696.

[5] L.J. Fortier, "An application of a proposed airdrop planning system," S.M. thesis, Massachusetts Institute of Technology, 2004.

[6] J. Neuhaus and P. Kenney, "A generic multibody parachute simulation model," in *AIAA Modeling and Simulation Technologies Conference*, 2006, AIAA Paper 2006-6622; doi: 10.2514/6.2006-6622.

[7] D. Pérez Sánchez, "Study of a methodology for the flight simulation of ram-air parachutes using a vortex-lattice aerodynamic model," Bachelor's thesis, Universitat Politècnica de Catalunya, 2017.

[8] V.N. Dobrokhodov, O.A. Yakimenko, and C.J. Junge, "Six-degree-of-freedom model of a controlled circular parachute," *J. Aircr.*, vol. 40, no. 3, pp. 482–493, 2003, doi: 10.2514/2.3143.

[9] G. Guglieri, "Parachute-payload system flight dynamics and trajectory simulation," *Int. J. Aerosp. Eng.*, vol. 2012, no. 1, p. 182907, 2012, doi: 10.1155/2012/182907.

[10] E. González, C. Sacco, E. Ortega, and R. Flores, "Development of a 6-DoF simulator for analysis and evaluation of autonomous parafoil systems," International Center for Numerical Methods in Engineering (CIMNE), Tech. Rep. PI356, 2011.

[11] L. Yan, Y. Song, H. Wang, and Z. Shi, "Dynamics modeling and autonomous landing for flexible parafoil-vehicle multibody system," *IEEE Access*, vol. 11, pp. 43 945–43 961, 2023, doi: 10.1109/ACCESS.2023.3271861.

[12] J. Yang *et al.*, "Dual-loop linear active disturbance rejection control for parafoil airdrop systems in wind environment," *Aerosp. Sci. Technol.*, vol. 158, p. 109910, 2025, doi: 10.1016/j.ast.2024.109910.

[13] Z. Yu, H. Sun, Q. Sun, P. Tan, Z. Chen, and J. Qu, "Dynamic path planning for parafoil homing in surface wind disturbance environment," *IEEE Trans. Autom. Sci. Eng.*, vol. 22, pp. 15 045–15 059, 2025, doi: 10.1109/TASE.2025.3563071.

[14] L. Yan, Y. Song, H. Wang, Z. Shi, and Y. Song, "Dynamic trajectory planning for autonomous parafoil homing under wind disturbances," *Aerospace*, vol. 13, no. 3, p. 276, 2026, doi: 10.3390/aerospace13030276.

[15] J. Tao *et al.*, "Modeling and control of a powered parafoil in wind and rain environments," *IEEE Trans. Aerosp. Electron. Syst.*, vol. 53, no. 4, pp. 1642–1659, 2017, doi: 10.1109/ TAES.2017.2667838.

[16] L. Zhao, J. Tao, H. Sun, and Q. Sun, "Dynamic modelling of parafoil system based on aerodynamic coefficients identification," *Automatika*, vol. 64, no. 2, pp. 291–303, 2023, doi: 10.1080/00051144.2022.2145697.

[17] M. Yao, Z. Cao, R. Guo, M. Zhao, and Y. Chen, "Nonlinear velocity control strategy and trajectory planning for parafoils using a restricted 6-DOF model," *J. Aerosp. Eng.*, vol. 38, no. 4, p. 04025047, 2025, doi: 10.1061/JAEEEZ.ASENG-6072.

[18] G. Brown, R. Haggard, R. Almassy, R. Benney, and S. Dellicker, "The affordable guided airdrop system (AGAS)," in *15th AIAA Aerodynamic Decelerator Systems Technology Conference*, 1999, AIAA Paper 1999-1742; doi: 10.2514/6.1999-1742.

[19] Z. Wei, Y. Gao, and Z. Shao, "Autonomous parafoil system precision landing via closed-loop guidance and control considering six-degree-of-freedom model," in *AIAA SCITECH 2024 Forum*, 2024, AIAA Paper 2024-0316; doi: 10.2514/6.2024-0316.

[20] S. Doran, T. Souanef, and J. F. Whidborne, "Autonomous parafoil flaring control system for eVTOL aircraft," *Aerospace*, vol. 12, no. 2, p. 145, 2025, doi: 10.3390/aerospace12020145.

[21] Z. Wei, K. Wang, Z. Shao, and L.T. Biegler, "Coordinated guidance and control for multiple parafoil system landing," *Adv. Space Res.*, vol. 77, no. 10, pp. 10 727–10 742, 2026, doi: 10.1016/j.asr.2026.02.059.

[22] H. Shah, N.D. Sathyanarayana, M. Ang, S. Sen, L. Gomez, and G. Olivares, "Aerodynamic performance evaluation of a small UAS using multi-fidelity numerical analyses," in *AIAA SCITECH 2025 Forum*, 2025, AIAA Paper 2025-0024; doi: 10.2514/6.2025-0024.

[23] FOXTECH, *Great Shark 330 VTOL User Manual*, 2019, version 1.0.

[24] P. Lissaman and G. Brown, "Apparent mass effects on parafoil dynamics," in *AIAA Aerospace Design Conference*, 1993, AIAA Paper 93-1236; doi: 10.2514/6.1993-1236.

[25] G. Kowaleczko, "Apparent masses and inertia moments of the parafoil," *J. Theor. Appl. Mech.*, vol. 52, no. 3, pp. 605–616, 2014.

[26] Z. Zhang, Z. Zhao, and Y. Fu, "Dynamics analysis and simulation of six DOF parafoil system," *Cluster Comput.*, vol. 22, no. 5, pp. 12 669–12 680, 2019, doi: 10.1007/s10586-018-1720-3.

[27] N. Slegers and M. Costello, "Model predictive control of a parafoil and payload system," *J. Guid. Control Dyn.*, vol. 28, no. 4, pp. 816–821, 2005, doi: 10.2514/1.12251.

[28] Y. Fu, W. An, X. Su, and B. Song, "Real-time wind estimation for fixed-wing UAVs," *Drones*, vol. 9, no. 8, p. 563, 2025, doi: 10.3390/drones9080563.

[29] M.R. Cacan, E. Scheuermann, M. Ward, M. Costello, and N. Slegers, "Autonomous airdrop systems employing ground wind measurements for improved landing accuracy," *IEEE/ASME Trans. Mechatron.*, vol. 20, no. 6, pp. 3060–3070, 2015, doi: 10.1109/ TMECH.2015.2405851.

[30] S. Park, J. Deyst, and J.P. How, "A new nonlinear guidance logic for trajectory tracking," in *AIAA Guidance, Navigation, and Control Conference and Exhibit*, 2004, AIAA Paper 2004-4900; doi: 10.2514/6.2004-4900.

[31] N. Slegers and M. Costello, "Aspects of control for a parafoil and payload system," *J. Guid. Control Dyn.*, vol. 26, no. 6, pp. 898–905, 2003, doi: 10.2514/2.6933.

[32] Windy, "Windy weather forecast," 2025. [Online]. Available: https://www.windy.com (Accessed 2025-06-20).